

LETTER TO THE EDITOR

H₃⁺ absorption and emission in local (U)LIRGs with JWST/NIRSpec: Evidence for high H₂ ionization rates

Miguel Pereira-Santaella^{1,*}, Eduardo González-Alfonso², Ismael García-Bernete^{3,4}, Fergus R. Donnan⁴, Miriam G. Santa-Maria⁵, Javier R. Goicoechea¹, Isabella Lamperti^{6,7}, Michele Perna⁸, and Dimitra Rigopoulou^{4,9}

(Affiliations can be found after the references)

Received 31 July 2024 / Accepted 25 August 2024

ABSTRACT

We study the $3.4-4.4\,\mu\text{m}$ fundamental rovibrational band of H_3^+ , a key tracer of the ionization of the molecular interstellar medium (ISM), in a sample of 12 local ($d < 400\,\text{Mpc}$) (ultra)luminous infrared galaxies ((U)LIRGs) observed with JWST/NIRSpec. The P, Q, and R branches of the band are detected in 13 out of 20 analyzed regions within these (U)LIRGs, which increases the number of extragalactic H_3^+ detections by a factor of 6. For the first time in the ISM, the H_3^+ band is observed in emission; we detect this emission in three regions. In the remaining ten regions, the band is seen in absorption. The absorptions are produced toward the $3.4-4.4\,\mu\text{m}$ hot dust continuum rather than toward the stellar continuum, indicating that they likely originate in clouds associated with the dust continuum source. The H_3^+ band is undetected in Seyfert-like (U)LIRGs where the mildly obscured X-ray radiation from the active galactic nuclei might limit the abundance of this molecule. For the detections, the H_3^+ abundances, $N(H_3^+)/N_H = (0.5-5.5) \times 10^{-7}$, imply relatively high ionization rates, ζ_{H_2} , of between 3×10^{-16} and $>4 \times 10^{-15} \, \text{s}^{-1}$, which are likely associated with high-energy cosmic rays. In half of the targets, the absorptions are blueshifted by $50-180\,\text{km s}^{-1}$, which is lower than the molecular outflow velocities measured using other tracers such as OH 119 μ m or rotational CO lines. This suggests that H_3^+ traces gas close to the outflow-launching sites before it has been fully accelerated. We used nonlocal thermodynamic equilibrium models to investigate the physical conditions of these clouds. In seven out of ten objects, the H_3^+ excitation is consistent with inelastic collisions with H_2 in warm translucent molecular clouds ($T_{kin} \sim 250-500\,\text{K}$ and $n(H_2) \sim 10^{2-3}\,\text{cm}^{-3}$). In three objects, dominant infrared pumping excitation is required to explain the absorptions from the (3,0) and (2,1) levels of H_3^+ detected for

Key words. cosmic rays - ISM: molecules - galaxies: active - galaxies: starburst - infrared: ISM

1. Introduction

Galaxies with high infrared (IR) luminosities ($L_{\rm IR} > 10^{11.5} L_{\odot}$), known as luminous and (ultra)luminous infrared galaxies ((U)LIRGs), are mostly gas-rich major mergers at different evolutionary stages (e.g., Hung et al. 2014). They represent a key phase in the evolution of galaxies both locally and at high z (e.g., Rodriguez-Gomez et al. 2015). (U)LIRGs host the strongest starbursts in the local Universe, with starformation rates of $>30-70\,M_\odot\,\mathrm{yr}^{-1}$, and many of them contain bright active galactic nuclei (AGN) as well (e.g., Veilleux et al. 2009; Nardini et al. 2010). (U)LIRGs also host massive molecular outflows with mass-outflow rates of up to $300 M_{\odot} \,\mathrm{yr}^{-1}$ (González-Alfonso et al. 2017; Lutz et al. 2020; Lamperti et al. 2022), which are expected to significantly influence their evolution by depleting the gas available for star formation and for fueling the central black hole. Most of the activity of (U)LIRGs takes place in compact ($d < 200 \,\mathrm{pc}$; Barcos-Muñoz et al. 2017; Pereira-Santaella et al. 2021) deeply dust-embedded cores $(N_{\rm H} > 10^{24}\,{\rm cm}^{-2};~{\rm Gonz\'alez}\text{-Alfonso et al.}~2015;~{\rm Falstad et al.}$ 2021; García-Bernete et al. 2022a; Donnan et al. 2023). These environments show a rich molecular gas chemistry, especially in the most obscured cases (e.g., González-Alfonso et al. 2012; Costagliola et al. 2015; Gorski et al. 2023). Cosmic rays have been proposed as the primary driver of the ionization and chemistry in these objects, as UV photons are shielded at high column densities. Additionally, cosmic rays can influence the conditions for star formation by heating the cores of dense molecular clouds (Papadopoulos 2010; Padovani et al. 2020).

In cosmic-ray-dominated regions (CRDRs), H_3^+ is a key molecule, initiating the interstellar chemistry by donating a proton to other atoms and molecules (e.g., Oka 2013). The H_3^+ formation is closely linked to the H_2 ionization rate, ζ_{H_2} : after the ionization of an H_2 molecule, H_2^+ readily reacts with another H_2 molecule to form H_3^+ . Its formation–destruction balance is relatively simple, particularly in diffuse clouds ($n(H_2) \sim 10^2 \, \text{cm}^{-3}$; e.g., Dalgarno 2006), and so H_3^+ has been used to measure ζ_{H_2} in Galactic regions. H_3^+ is also abundant in X-ray-dominated regions (XDRs) when the X-ray radiation field has been sufficiently attenuated (Maloney et al. 1996). Thus, for objects with an AGN, the H_3^+ abundance can be affected by the X-ray radiation too.

Galactic H_3^+ absorptions have been detected toward the Galactic center (GC), dense molecular clouds, and diffuse clouds using ground-based observations (e.g., Geballe & Oka 1996; McCall et al. 2002; Goto et al. 2008; Gibb et al. 2010). In these environments, ζ_{H_2} varies between $\sim 10^{-17} \, \text{s}^{-1}$ in dense clouds (McCall et al. 1999), $\sim 10^{-16} \, \text{s}^{-1}$ in diffuse clouds (Indriolo & McCall 2012), and $\sim 10^{-14} \, \text{s}^{-1}$ in the GC (Le Petit et al. 2016; Oka et al. 2019). Two extragalactic H_3^+ detections have been reported so far: in the ULIRG IRAS 08572+3915 NW (Geballe et al. 2006; which is also part

 $^{^\}star$ Corresponding author; miguel.pereira@iff.csic.es

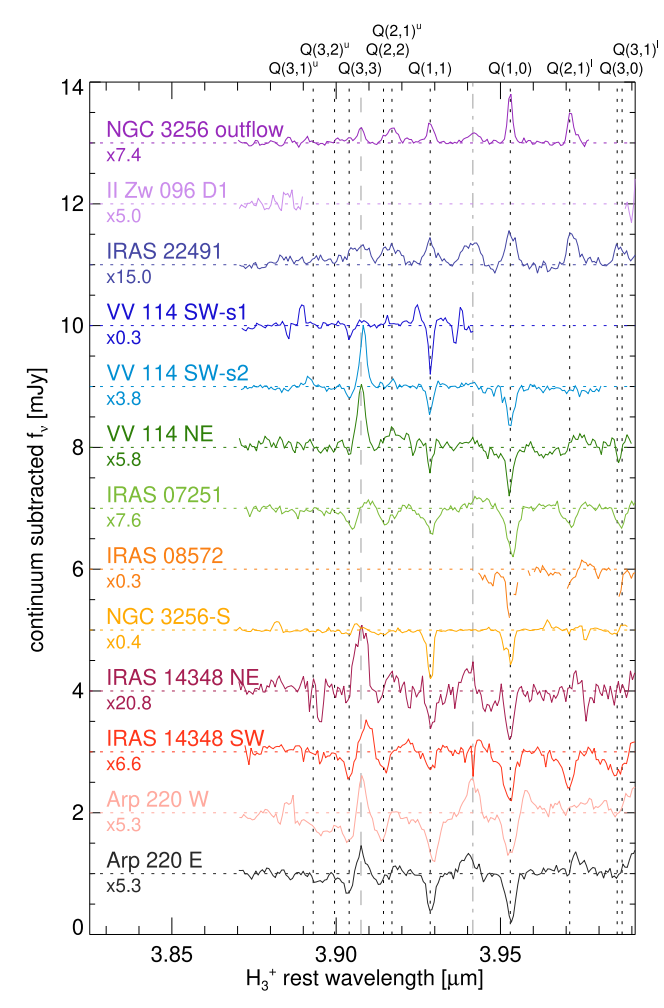


Fig. 1. *Q* branch of the fundamental rovibrational ν_2 band of H_3^+ (*P* and *R* branches are shown in Fig. C.1). The JWST/NIRSpec spectra are continuum-subtracted (Sect. 2.3) and scaled. The H_3^+ transitions are labeled at the top of the panel and indicated by the dotted black vertical lines. Dashed and dot-dashed gray vertical lines indicate transitions of H_2 and H_1 , respectively. The number below the region name is the scaling factor applied. In this figure, the rest frame is defined by the velocity of the H_3^+ features. We note that the JWST/NIRSpec spectra have a ~0.1 μ m gap centered around 4.05–4.15 μ m that partially affects the *Q* branch of some of these regions. For IRAS 08572, we masked spectral channels with highly uncertain flux values.

of the sample studied here), and a much fainter detection in the Type 2 AGN NGC 1068 (Geballe et al. 2015).

In this Letter, we analyze *James Webb* Space Telescope (JWST) Near IR Spectrograph (NIRSpec; Jakobsen et al. 2022) observations that cover the 3.4–4.4 μm spectral range where the H_3^+ fundamental rovibrational ν_2 band lies. We study the kinematics of the absorptions and measure the H_3^+ column densities. We also estimate ζ_{H_2} from the H_3^+ abundance and investigate the physical conditions of the clouds producing these absorptions using radiative transfer models. We used the spectroscopic parameters of H_3^+ from Mizus et al. (2017).

2. Analysis and results

We extracted the high-resolution ($R \sim 1900-3600$) JWST/NIRSpec spectra of 20 regions (nuclei and bright near-IR clumps) in 12 local (39–400 Mpc) (U)LIRGs with $L_{\rm IR} = 10^{11.6-12.5} L_{\odot}$. All these (U)LIRGs are interacting systems at dif-

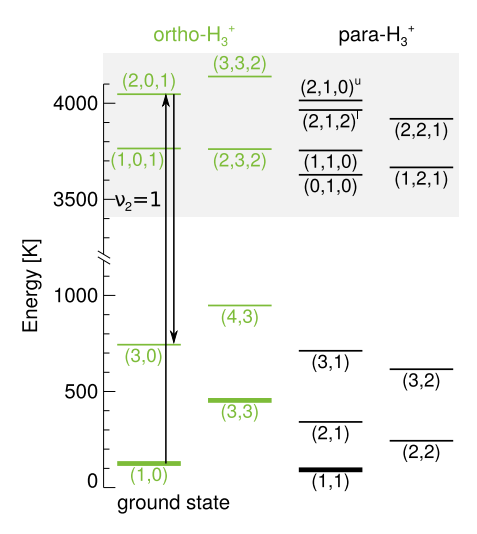


Fig. 2. Energy level diagram of H_3^+ . The gray shaded area marks the $v_2=1$ levels. Ortho- H_3^+ levels are in green and para- H_3^+ in black. The metastable and ground rotational levels are indicated by thicker lines. For the ground state, the quantum numbers of each level are (J,K) and for the $v_2=1$ levels, (J,G,K). The detected transitions connect the ground and the $v_2=1$ states. The arrows show how the (3,0) level can be populated by IR pumping through the R(1,0) and P(3,0) transitions.

ferent merger stages. The spectra were extracted using 0".40 diameter apertures (80–800 pc depending on the distance). More details on the sample and the data reduction are presented in Appendix A and Table A.1.

Figure 1 shows the Q branch of the fundamental v_2 band of H_3^+ in these objects (the P and R branches are shown in Fig. C.1). The H_3^+ band is detected in 13 out of the 20 sources analyzed (the nondetections are shown in Fig. C.2). It is seen in absorption in ten targets and, for the first time, this band is detected in emission from gas in the interstellar medium (ISM) in the nuclei of two U/LIRGs and the molecular outflow of another target. Previous detections of H_3^+ emission were limited to the giant gas and ice planets of the Solar System (e.g., Drossart et al. 1989; Trafton et al. 1993). In this Letter, we focus on the targets where the band is detected in absorption. The analysis of the emission bands will be presented in a future work (Pereira-Santaella et al. in prep.).

2.1. H₂ spectroscopy and Galactic observations

The energy level diagram of H_2^+ is shown in Fig. 2. There are two H_3^+ spin isomers depending on the total nuclear spin I: ortho- H_3^+ with I = 3/2 and quantum number K = 3n; and para- H_3^+ with I = 1/2 and $K = 3n \pm 1$ (green and black levels in Fig. 2, respectively). Due to the selection rules, the (3,3) level of the ground state is metastable and cannot decay radiatively to the lowest ortho-H₃⁺ level (1,0) (see e.g., Oka 2013; Miller et al. 2020 for a detailed description of the H_3^+ spectroscopy). Therefore, H_3^+ molecules tend to accumulate in the (1,1), (1,0), and (3,3) levels in the conditions of the ISM. More specifically, Galactic observations of H_3^+ in both diffuse and dense $(n(H_2) \sim 10^{4-5} \, \text{cm}^{-3})$ clouds detect only the (1,1) and (1,0) absorptions (McCall et al. 1999; Indriolo & McCall 2012), whereas the higher excitation (3,3) absorptions are observed only toward the GC. A (2,2) absorption has been uniquely detected along a line of sight (GC IRS 3) toward the circumnuclear disk (CND) of the GC (Goto et al. 2008, 2014; Oka et al. 2019).

2.2. H₃⁺ kinematics: Outflows and inflows

The absorptions were fitted using Gaussian profiles. As in Pereira-Santaella et al. (2024), we tied the line-of-sight velocity of all the H_3^+ transitions to a common value. We also tied the velocity dispersion of the transitions of the same branch, but allowed it to vary between the three branches to account for the variation of the resolving power of NIRSpec (see Appendix A).

In 50% of the sample (five objects), the $\rm H_3^+$ absorptions are blueshifted 50–180 km s⁻¹ relative to the molecular and ionized gas traced by the high-J pure rotational $\rm H_2$ and $\rm H$ recombination lines observed by NIRSpec. This indicates that the clouds with $\rm H_3^+$ are outflowing (Fig. A.1). These $\rm H_3^+$ outflow velocities are lower than those measured using the OH 119 μm and the CO(2–1) 230.5 GHz lines for these targets (\sim 300–500 km s⁻¹; Veilleux et al. 2013; Lamperti et al. 2022). Thus, it is possible that $\rm H_3^+$ traces clouds close to the outflow launching sites before the gas has been fully accelerated (e.g., González-Alfonso et al. 2017; Pereira-Santaella et al. 2020). Only in the southern nucleus of NGC 3256 are the $\rm H_3^+$ absorptions redshifted, by \sim 70–140 km s⁻¹, suggesting an inflow.

2.3. H₃⁺ column densities and location of the clouds

We estimated the column density of each H_3^+ level using the standard relation for optically thin lines:

$$N_l = \frac{8\pi c}{A_{ul}\lambda^4} \frac{g_l}{g_u} W_{\lambda},\tag{1}$$

where W_{λ} is the equivalent width (EW) in wavelength units of the absorptions, N_l the column density of the lower level, λ the wavelength of the transition, c the speed of light, $A_{\rm ul}$ the Einstein A-coefficient of the transition, and g_l and g_u the statistical weights of the lower and upper levels, respectively.

In order to measure W_{λ} , we used a spline-interpolated baseline to estimate the continuum level. We note that the EW of the P(2,2) and P(2,1) transitions (affected by the 4.27 μ m CO₂ ice and gas absorptions) and the R(3,3)^l and R(3,3)^u transitions (affected by the 3.4–3.6 μ m stellar continuum features and PAH aliphatic bands) are relatively uncertain.

We find that, for the same level, the column densities derived from the shorter wavelength branches are lower than those derived from longer wavelength branches. In particular, for the (1,1) and (3,3) levels, which show absorptions in two or three branches, the R branch (3.4–3.7 μ m) columns are, on average, \sim 1.5 times lower than those derived from the Q branch (3.9–4.0 μ m), and the latter are \sim 1.3 times lower than those derived from the P branch (4.2–4.4 μ m).

In these objects, the stellar continuum dominates the near-IR continuum up to ~3.5–3.9 μ m, while the hot-dust continuum dominates the spectra at longer wavelengths (Donnan et al. 2024). Thus, the column-density discrepancies can be explained if the H_3^+ absorptions are primarily produced toward the compact hot-dust continuum ($r < 20\,\mathrm{pc}$ in some of these objects; Rich et al. 2023; García-Bernete et al. 2024b; Inami et al. 2022), whereas the more spatially extended stellar continuum, not affected by the H_3^+ absorptions, reduces the observed EW at shorter wavelengths. This also implies that the spatial extent of the H_3^+ clouds is more similar to that of the compact dust continuum than to the extended stellar continuum. The nondetection of the $R(3,3)^u$ line at 3.43 μ m (where the stellar continuum dominates) in 9 out of 10 regions further corroborates the proposed explanation. $R(3,3)^u$ should have an EW that is >2–10

times higher than the derived upper limits based on the P(3,3) absorption at $4.35 \, \mu m$.

3. Discussion

3.1. H₂ Ionization rate: Cosmic rays and X-rays

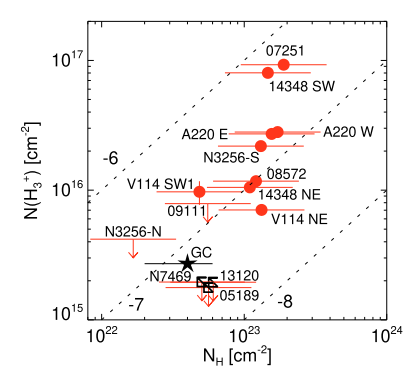
For low $\zeta_{\rm H_2}/n_{\rm H}$ (<10⁻¹⁷ cm³ s⁻¹), where $n_{\rm H}=n({\rm H})+2n({\rm H_2})$, the H₃⁺ abundance is proportional to $\zeta_{\rm H_2}/n_{\rm H}$. For higher $\zeta_{\rm H_2}/n_{\rm H}$, the molecular fraction, $f_{\rm H_2}=2n({\rm H_2})/n_{\rm H}$, decreases, reducing the formation rate of H₃⁺, and the increased abundance of free electrons, $x_{\rm e}$, enhances the dissociative recombinations of H₃⁺. Hence, in this limit, the H₃⁺ abundance decreases for increasing $\zeta_{\rm H_2}/n_{\rm H}$ in both XDR and CRDR (see Maloney et al. 1996; Le Petit et al. 2016; Neufeld & Wolfire 2017).

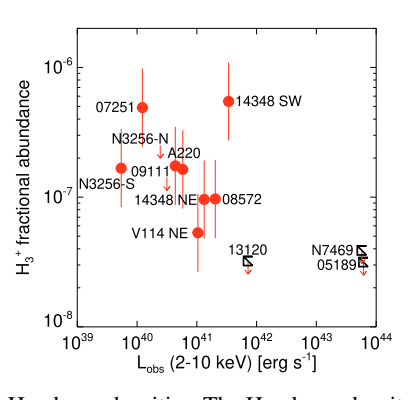
Thus, as a first step to estimate ζ_{H_2} , we calculated the H_3^+ fractional abundance, $N(H_3^+)/N_H$. We estimated N_H from the extinction affecting the $3.4-4.4 \,\mu m$ continuum where the H_3^+ absorptions are detected. This is justified because the H₃⁺ absorptions are produced in clouds close to the continuum source (Sect. 3.2), which are likely the same clouds that extinguish this 3.4–4.4 µm continuum. We used the method presented by Donnan et al. (2024) to model the differential extinction of the 3–28 µm continuum observed with NIRSpec and MIRI/MRS for these sources. We obtain an extinction at \sim 4 μm equivalent to $N_{\rm H}$ $(2-19)\times 10^{22}$ cm $^{-2}$ (Table B.4). This is approximately equivalent to an optical depth $\tau_{4\mu m}$ of about ~0.4–5¹. Higher $\tau_{4\mu m}$ would make this $3.4-4.4 \mu m$ dust continuum too weak to be detected. However, we note that the $N_{\rm H}$ affecting the longer-wavelength continuum in these (U)LIRGs is considerably larger due to differential extinction effects.

Figure 3 shows that, for the detections, the average H₃⁺ abundance is $\sim 2 \times 10^{-7}$, which is slightly higher than the average abundance in the GC, of namely $\sim 0.7 \times 10^{-7}$ (Oka et al. 2019). Interestingly, the $N(H_3^+)$ upper limits for the three Sy AGN, that is, the less-obscured AGN in the sample where high-ionization lines are detected, imply low H_3^+ abundances $<4 \times 10^{-8}$. This result is also consistent with the low H₃⁺ EW measured in the Sy 2 AGN NGC 1068 (Geballe et al. 2015). This can be explained if the X-ray radiation from the AGN induces a sufficiently high $\zeta_{\rm H_2}$ to suppress the formation of ${\rm H_3^+}$ by both decreasing $f_{\rm H_2}$ and increasing x_e . The middle panel of Fig. 3 shows the relation between the observed 2–10 keV X-ray luminosity, $L_{\rm obs}(2 10\,\text{keV}$), and the H_3^+ abundance. The three Sy AGN have the highest $L_{\rm obs}(2-10\,{\rm keV})$ and the most stringent upper limits on the H₃⁺ abundance. This suggests that X-rays might be limiting the formation of H_3^+ . We also estimated ζ_{H_2} due to X-rays by combining Eqs. 12 and 15 from Maloney et al. (1996). For an $N_{\rm H}$ of 10^{23} cm⁻², $\zeta_{\rm H_2}/{\rm s}^{-1} = 1.9 \times 10^{-14} \ F_{\rm x}/({\rm erg \ s}^{-1} \ {\rm cm}^{-2})$, where $F_{\rm x}$ is the incident X-ray flux. Therefore, an observed X-ray luminosity of 10^{43} erg s⁻¹ –which is similar to that of the brightest Sy AGN in the sample– at 50 pc implies $\zeta_{\rm H_2} \sim 6 \times 10^{-13} \, {\rm s}^{-1}$, which for the average $n({\rm H_2})$ of $10^{2-3} \, {\rm cm}^{-3}$ (Sect. 3.2) can place these objects in the regime where the H₃⁺ abundance decreases with increasing $\zeta_{\rm H_2}$ (right side of the right panel of Fig. 3).

In this section we use the observed instead of the intrinsic X-ray luminosities because the H_3^+ absorptions originate at the outer obscuring layers ($N_{\rm H} \sim 10^{23} \, {\rm cm}^{-2}$) in objects with a total $N_{\rm H}$ of up to $10^{25} \, {\rm cm}^{-2}$, and thus a significant part of the intrinsic X-ray emission has likely been absorbed by more internal gas and dust layers.

 $^{^1}$ For a screen extinction law $N_{\rm H}/\tau_{4\mu m}\sim 3.8\times 10^{22}$ cm $^{-2}$ (Bohlin et al. 1978; Chiar & Tielens 2006).





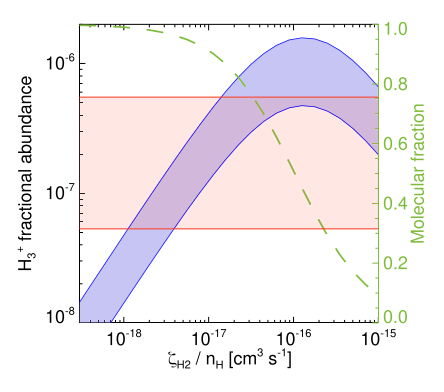


Fig. 3. H_3^+ fractional abundance. Left panel: H_3^+ vs. H column densities. The H column density corresponds to the obscuring material of the ~4 μm continuum derived from the continuum differential extinction model (Sect. 3.1). The dashed lines indicate constant H_3^+ fractional abundances between 10^{-6} and 10^{-8} in steps of 1 dex. The red circles are the observed (U)LIRGs. The black star corresponds to the average columns in the GC from Goto et al. (2008) and Oka et al. (2019). Upper limits for Seyfert-type AGN are indicated by the empty black squares. Middle panel: H_3^+ fractional abundance as a function of the observed 2–10 keV X-ray luminosity. Right panel: Blue shaded area is the predicted H_3^+ fractional abundance (left y-axis) as a function of ζ_{H_2}/n_H estimated using Eq. 2 from Neufeld & Wolfire (2017) for x_e in the range (1.5–5) × 10^{-4} (Sect. 3.1). The horizontal red shaded area indicates the range of H_3^+ fractional abundances measured in these (U)LIRGs. The dashed green line (right y-axis) is f_{H_2} as function of ζ_{H_2}/n_H using Eq. 2 from González-Alfonso et al. (2013).

The right panel of Fig. 3 shows the predicted H_3^+ abundance as a function of $\zeta_{\mathrm{H_2}}/n_{\mathrm{H}}$ derived using Eq. 2 from Neufeld & Wolfire (2017) at $T=300\,\mathrm{K}$. Following González-Alfonso et al. (2013), we assumed x_{e} in the range (1.5–5)×10⁻⁴ and $f_{\mathrm{H_2}}$ given by their Eq. 2. This simplified approximation ignores most of the H_3^+ chemical reactions, but captures the two key elements, x_{e} and $f_{\mathrm{H_2}}$, which determine its abundance in diffuse and translucent clouds (Dalgarno 2006; Shaw & Ferland 2021). From the H_3^+ fractional abundance of the (U)LIRGs, $(0.5–5.5)\times10^{-7}$, we estimate a $\zeta_{\mathrm{H_2}}/n_{\mathrm{H}}$ of between 10^{-18} and $>1.3\times10^{-17}\,\mathrm{cm}^3\,\mathrm{s}^{-1}$. The average $n(\mathrm{H_2})$ is $\sim10^{2.5}\,\mathrm{cm}^{-3}$ (Sect. 3.2), and so the resulting $\zeta_{\mathrm{H_2}}$ are between $\sim3\times10^{-16}$ and $>4\times10^{-15}\,\mathrm{s}^{-1}$.

The origin of the H₃⁺ detections –either X-rays or cosmic rays- is difficult to constrain. The effects of both X-rays and cosmic rays on the gas are similar (e.g., Glassgold et al. 2012; Wolfire et al. 2022). Here, we consider the fact that cosmic rays can penetrate much larger column densities than X-rays. Therefore, if X-ray radiation from an AGN is present in these (U)LIRGs, it would be absorbed by the internal gas layers, preventing it from reaching the more external gas clouds. This hypothesis is supported by observations showing that (U)LIRGs are under-luminous in hard X-rays (Imanishi & Terashima 2004; Teng et al. 2015; Ricci et al. 2021). Similarly, low-energyproton cosmic rays (<10-100 MeV) have stopping ranges of below 10^{24} cm⁻² (Padovani et al. 2018), and so they are likely absorbed by the internal gas layers too. However, cosmic rays of more energetic protons (100–180 MeV), with stopping ranges of 10^{24–25} cm⁻², can deposit their energy over large columns comparable to those of (U)LIRGs. Therefore, we consider that ionization by >100 MeV cosmic rays is more plausible than X-ray ionization in these objects. These cosmic rays are more energetic than those in our Galaxy, which have typical energies of 2-10 MeV (Indriolo et al. 2009). Thus, depending on both the cosmic-ray energy spectrum and the total N_H of (U)LIRGs, the intrinsic cosmic-ray luminosity can be >20 times² higher than in the GC for the same $\zeta_{\rm H_2}$.

Other molecular ions like OH^+ , H_2O^+ , and H_3O^+ , which can form via reactions with H_3^+ , have been detected in (U)LIRGs hosting Seyfert AGN (including NGC 7469, which is part of this sample; van der Werf et al. 2010; Aalto et al. 2011; Pereira-Santaella et al. 2013, 2014). The low H_3^+ abundance in these AGN supports the idea that these ions form through reaction chains involving H^+ and O^+ , instead of H_3^+ (Hollenbach et al. 2012; González-Alfonso et al. 2013; Gómez-Carrasco et al. 2014).

3.2. Physical conditions of the H₃⁺ clouds

Previous studies of the H₃⁺ absorptions toward the GC indicate that H₃⁺ traces a warm ($T \sim 200{\text -}500\,\text{K}$) diffuse ($n_{\rm H} < 100\,\text{cm}^{-3}$) gas phase with a high cosmic-ray ionization rate ($\zeta_{\rm cr} \sim (1{\text -}10) \times 10^{-14}\,\text{s}^{-1}$; Goto et al. 2008; Le Petit et al. 2016; Oka et al. 2019). In this section, we investigate the similarity between the conditions in these (U)LIRGs and those of the GC.

A major difference is that the observed H_3^+ column densities in these objects, $N(H_3^+) = (7-93) \times 10^{15} \, \mathrm{cm}^{-2}$, are 2–30 times higher than in the GC. The H_3^+ excitation is also different in some objects. Figure 4 shows column density ratios between various H_3^+ levels that can be used to characterize the physical conditions of these clouds (e.g., Goto et al. 2008; Le Petit et al. 2016). As shown in the top panel of Fig. 4, contrary to Galactic diffuse and dense clouds, the (3,3) lines are detected in all these (U)LIRGs. Thus, this ratio also suggests that the detections in (U)LIRGs are not produced in extended diffuse gas halos (see also Sect. 2.3).

In Fig. 4, we also plot a grid of nonlocal thermodynamic equilibrium (NLTE) models calculated using RADEX (van der Tak et al. 2007) with the H_3^+ – H_2 collisional coefficients from Oka & Epp (2004). The RADEX grid covers H_2 densities, $\log n(H_2)/\text{cm}^{-3}$, of between 1.0 and 6.0, and kinetic temperatures, T_{kin} , of between 15 and 600 K in logarithmic steps.

In three targets, VV 114 NE and SW-s1, and IRAS 14348-NE, the (2,2) absorptions are not detected and the ratios are similar to those in the GC. Thus, for these nuclei, the gas temperature is 150–300 K and $n(\rm H_2)$ < 100 cm⁻³, which are comparable to those of the GC (Goto et al. 2008; Le Petit et al. 2016; Oka et al. 2019). We note that some of the observed (1,0)/(1,1) ratios are not well reproduced by these NLTE grids (top panel of Fig. 4). The formation of $\rm H_3^+$ is highly exothermic

² This factor is the ratio between the effective $\zeta_{\rm H_2}$ for $N_{\rm H}=10^{22}\,{\rm cm}^{-2}$ and $10^{25}\,{\rm cm}^{-2}$ given by Eq. F.1 of Padovani et al. (2018) for the cosmic-ray energy spectrum \mathscr{H} .

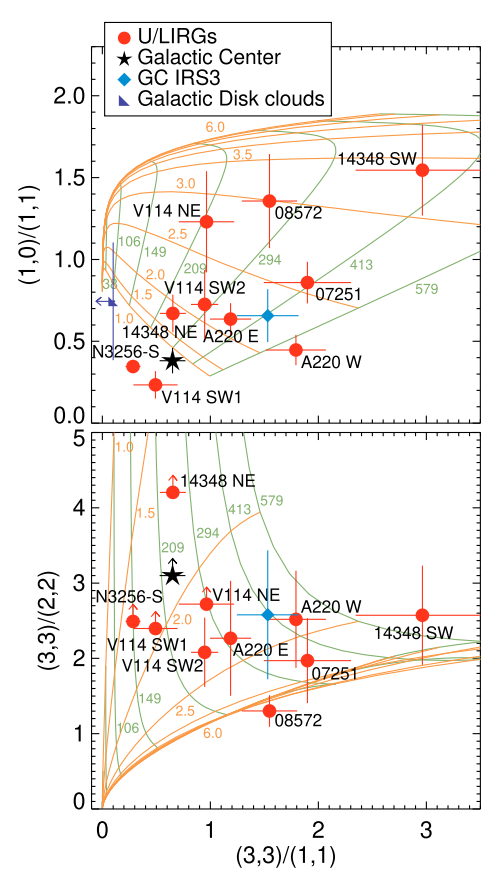


Fig. 4. Ratio between the column densities of H_3^+ levels: (1,0)/(1,1) vs. (3,3)/(1,1) (top); and (3,3)/(2,2) vs. (3,3)/(1,1) (bottom). Symbols as in Fig. 3. The blue diamond corresponds to the excited GC IRS 3 line of sight toward the GC, and the dark blue square in the top panel to diffuse and dense molecular clouds in the Galactic disk. The background grids show the ratios predicted by NLTE models. The green (orange) lines mark the ratios for the temperature, in K, (density, in $\log \, \mathrm{cm}^{-3}$) indicated by the colored labels.

 $(1.74 \,\mathrm{eV} \equiv 20190 \,\mathrm{K})$ and this can affect the observed populations of the (1,0) and (1,1) levels, which do not always reach the ortho-para thermal equilibrium (Le Bourlot et al. 2024). Therefore, formation pumping might explain the low (1,0)/(1,1) ratio in some of these regions. The remaining targets have clear (2,2) detections. For most objects, the (3,3)/(2,2) ratios (bottom panel of Fig. 4) are comparable, within the uncertainties, with that of the singular GC IRS 3 line of sight (Goto et al. 2008, 2014), and indicate warmer ($T_{\rm kin} = 250{-}500 \,\mathrm{K}$) and denser ($\log n(\mathrm{H_2}) = 10^{2-3} \,\mathrm{cm}^{-3}$) clouds.

Some absorptions cannot be explained by these NLTE models. In particular, the absorptions from the (3,0) and (2,1) levels, detected in IRAS 07251, IRAS 08572, and IRAS 14348-SW (Table B.4), are 5–50 times stronger than those predicted by the best-fit NLTE models. However, these absorptions can be explained by IR pumping. When the IR pumping rate, which is proportional to the ambient IR radiation field ϕ_{IR} , is higher than the collisional rate, which is proportional to $n(H_2)$, the (3,0) level, and similarly the (2,1) level, can be populated by the mechanism shown in Fig. 2 (see also Sect. 5.5 in Goto et al. 2008). Therefore, in these three objects, the $\phi_{IR}/n(H_2)$ ratio is likely sufficiently high to make IR pumping the dominant excitation mechanism. We verified this scenario by creating a grid of full radiative transfer models, including the effects of IR pumping, which are able to reproduce these absorptions (Appendix D).

4. Summary and conclusions

We analyzed the fundamental $3.4-4.4\,\mu m$ rovibrational band of H_3^+ in the spectra of 20 regions (nuclei and bright clumps) selected in 12 local ($d\sim39-400\,\mathrm{Mpc}$) (U)LIRGs observed by JWST/NIRSpec. The H_3^+ band is detected in 13 out of 20 regions. It is seen in emission for the first time in the ISM in three of these regions, and in absorption in the remaining ten regions. The main results from our analysis of the H_3^+ absorptions are as follows:

- 1. H_3^+ cloud location. The H_3^+ absorptions are primarily produced toward the hot dust continuum, which dominates the spectra at >3.5–3.9 μ m, rather than toward the stellar continuum. Consequently, the clouds traced by these H_3^+ absorptions are likely associated with the compact ($r < 20 \,\mathrm{pc}$ in some cases) dust continuum source.
- 2. Nondetection of H_3^+ in Seyfert AGN. The H_3^+ absorptions are undetected in the Seyfert-like (U)LIRGs. These objects are among those least obscured in the sample. Thus, they host mildly obscured AGN whose X-ray radiation might be limiting the abundance of H_3^+ by decreasing the molecular fraction f_{H_2} and increasing the free electron abundance x_e .
- 3. Low-velocity molecular outflows and inflows. In five regions (50% of the sample), the H_3^+ absorptions are blueshifted by 50–180 km s $^{-1}$ relative to the ionized and warm/hot molecular gas. These outflow velocities are lower than those measured using OH 119 μm or rotational CO lines in these objects. This suggests that H_3^+ traces clouds closer to the outflow launching sites before it has been fully accelerated. In one region, the absorptions are redshifted by 70–140 km s $^{-1}$ suggesting inflowing gas.
- 4. H_3^+ column densities, abundances, and H_2 ionization rate. The H_3^+ column densities are $(0.7-9.3)\times 10^{16}\,\mathrm{cm}^{-2}$, which corresponds to fractional H_3^+ abundances of $(0.5-5.5)\times 10^{-7}$. Using a simple model for H_3^+ abundance in translucent clouds, we estimate $\zeta_{\rm H_2}/n_{\rm H}$ to be between 10^{-18} and $>1.3\times 10^{-17}\,\mathrm{cm}^3\,\mathrm{s}^{-1}$. For $n({\rm H_2})\sim 10^{2.5}\,\mathrm{cm}^{-3}$ (see below), $\zeta_{\rm H_2}$ are between 3×10^{-16} and $>4\times 10^{-15}\,\mathrm{s}^{-1}$. Energetic cosmic rays with $E>100-180\,\mathrm{MeV}$ have stopping ranges of $N_{\rm H}\sim 10^{24-25}\,\mathrm{cm}^{-2}$, comparable to the total $N_{\rm H}$ of (U)LIRGs, and so they are a plausible origin for these $\zeta_{\rm H_2}$.
- 5. NLTE models and excitation of H_3^+ . We find that in most of the regions that show H_3^+ absorption (seven out of ten), the H_3^+ excitation is consistent with warm translucent molecular clouds ($T_{\rm kin} \sim 250\text{--}500\,\mathrm{K}$ and $n(H_2) \sim 10^{2-3}\,\mathrm{cm}^{-3}$) excited by inelastic collisions with H_2 . These conditions are similar to those observed in the extreme line-of-sight GC IRS 3 toward the CND of the GC. In three objects, absorptions from the (3,0) and (2,1) levels of o- H_3^+ and p- H_3^+ , respectively, are detected for the first time in the ISM. These objects require IR pumping excitation to explain these excited absorptions.

These results show the potential of JWST to detect the key molecule H_3^+ in extragalactic objects. This will allow constraint of the ionization and chemistry of the molecular ISM (i.e., the initial conditions for star formation) using H_3^+ for the first time in large samples of galaxies.

Acknowledgements. We are grateful to Octavio Roncero for insightful discussions about $\rm H_3^+$ and reading the manuscript. We thank the referee, David Neufeld, for a careful reading of the manuscript and a constructive report. The authors acknowledge the GOALS and the NIRSpec GTO teams for developing their observing programs. MPS acknowledges support under grants RYC2021-033094-I and CNS2023-145506 funded by MCIN/AEI/10.13039/501100011033 and the European Union NextGenerationEU/PRTR. MPS, EGA, MGSM, and JRG acknowledge funding support under grant PID2023-146667NB-I00 funded

by the Spanish MCIN/AEI/10.13039/501100011033. EGA acknowledges grants PID2019-105552RB-C4 and PID2022-137779OB-C41 funded by the Spanish MCIN/AEI/10.13039/501100011033. IGB is supported by the Programa Atracción de Talento Investigador "César Nombela" via grant 2023-T1/TEC-29030 funded by the Community of Madrid. FD acknowledges support from STFC through studentship ST/W507726/1. MGSM acknowledges support from the NSF under grant CAREER 2142300. MP acknowledges grant PID2021-127718NB-I00 funded by the Spanish Ministry of Science and Innovation/State Agency of Research (MICIN/AEI/ 10.13039/501100011033). DR acknowledges support from STFC through grants ST/S000488/1 and ST/W000903/1. This work is based on observations made with the NASA/ESA/CSA James Webb Space Telescope. The data were obtained from the Mikulski Archive for Space Telescopes at the Space Telescope Science Institute, which is operated by the Association of Universities for Research in Astronomy, Inc., under NASA contract NAS 5-03127 for JWST; and from the European JWST archive (eJWST) operated by the ESAC Science Data Centre (ESDC) of the European Space Agency. These observations are associated with programs #1267, #1328 and #3368.

References

```
Aalto, S., Costagliola, F., van der Tak, F., & Meijerink, R. 2011, A&A, 527, A69
Argyriou, I., Glasse, A., Law, D. R., et al. 2023, A&A, 675, A111
Armus, L., Mazzarella, J. M., Evans, A. S., et al. 2009, PASP, 121, 559
Armus, L., Lai, T., Vivian, U., et al. 2023, ApJ, 942, L37
Barcos-Muñoz, L., Leroy, A. K., Evans, A. S., et al. 2017, ApJ, 843, 117
Bianchin, M., Vivian, U., Song, Y., et al. 2024, ApJ, 965, 103
Blustin, A. J., Branduardi-Raymont, G., Behar, E., et al. 2003, A&A, 403, 481
Bohlin, R. C., Savage, B. D., & Drake, J. F. 1978, ApJ, 224, 132
Böker, T., Arribas, S., Lützgendorf, N., et al. 2022, A&A, 661, A82
Buiten, V. A., van der Werf, P. P., Viti, S., et al. 2024, ApJ, 966, 166
Bushouse, H., Eisenhamer, J., Dencheva, N., et al. 2023, JWST Calibration
   Pipeline https://doi.org/10.5281/zenodo.7829329
Chiar, J. E., & Tielens, A. G. G. M. 2006, ApJ, 637, 774
Clements, D. L., McDowell, J. C., Shaked, S., et al. 2002, ApJ, 581, 974
Costagliola, F., Sakamoto, K., Muller, S., et al. 2015, A&A, 582, A91
Dalgarno, A. 2006, Proc. Nat. Acad. Sci., 103, 12269
Donnan, F. R., García-Bernete, I., Rigopoulou, D., et al. 2023, MNRAS, 519,
Donnan, F. R., García-Bernete, I., Rigopoulou, D., et al. 2024, MNRAS, 529,
   1386
Drossart, P., Maillard, J. P., Caldwell, J., et al. 1989, Nature, 340, 539
Duc, P. A., Mirabel, I. F., & Maza, J. 1997, A&AS, 124, 533
Falstad, N., Aalto, S., König, S., et al. 2021, A&A, 649, A105
García-Bernete, I., Rigopoulou, D., Aalto, S., et al. 2022a, A&A, 663, A46
García-Bernete, I., Rigopoulou, D., Alonso-Herrero, A., et al. 2022b, A&A, 666,
   1.5
García-Bernete, I., Rigopoulou, D., Alonso-Herrero, A., et al. 2022c, MNRAS,
   509, 4256
García-Bernete, I., Alonso-Herrero, A., Rigopoulou, D., et al. 2024a, A&A, 681,
   L.7
García-Bernete, I., Pereira-Santaella, M., González-Alfonso, E., et al. 2024b,
Geballe, T. R., & Oka, T. 1996, Nature, 384, 334
Geballe, T. R., Goto, M., Usuda, T., Oka, T., & McCall, B. J. 2006, ApJ, 644,
Geballe, T. R., Mason, R. E., & Oka, T. 2015, ApJ, 812, 56
Gibb, E. L., Brittain, S. D., Rettig, T. W., et al. 2010, ApJ, 715, 757
Glassgold, A. E., Galli, D., & Padovani, M. 2012, ApJ, 756, 157
Gómez-Carrasco, S., Godard, B., Lique, F., et al. 2014, ApJ, 794, 33
González-Alfonso, E., Cernicharo, J., van Dishoeck, E. F., Wright, C. M., &
   Heras, A. 1998, ApJ, 502, L169
González-Alfonso, E., Fischer, J., Graciá-Carpio, J., et al. 2012, A&A, 541, A4
González-Alfonso, E., Fischer, J., Bruderer, S., et al. 2013, A&A, 550, A25
González-Alfonso, E., Fischer, J., Sturm, E., et al. 2015, ApJ, 800, 69
González-Alfonso, E., Fischer, J., Spoon, H. W. W., et al. 2017, ApJ, 836, 11
González-Alfonso, E., García-Bernete, I., Pereira-Santaella, M., et al. 2024,
   A&A, 682, A182
Gorski, M. D., Aalto, S., König, S., et al. 2023, A&A, 670, A70
Goto, M., Usuda, T., Nagata, T., et al. 2008, ApJ, 688, 306
Goto, M., Geballe, T. R., Indriolo, N., et al. 2014, ApJ, 786, 96
Grimes, J. P., Heckman, T., Hoopes, C., et al. 2006, ApJ, 648, 310
Hollenbach, D., Kaufman, M. J., Neufeld, D., Wolfire, M., & Goicoechea, J. R.
   2012, ApJ, 754, 105
Hung, C.-L., Sanders, D. B., Casey, C. M., et al. 2014, ApJ, 791, 63
Imanishi, M., & Terashima, Y. 2004, AJ, 127, 758
Inami, H., Surace, J., Armus, L., et al. 2022, ApJ, 940, L6
```

```
Jakobsen, P., Ferruit, P., Alves de Oliveira, C., et al. 2022, A&A, 661, A80
Labiano, A., Argyriou, I., Álvarez-Márquez, J., et al. 2021, A&A, 656, A57
Lamperti, I., Pereira-Santaella, M., Perna, M., et al. 2022, A&A, 668, A45
Le Bourlot, J., Roueff, E., Le Petit, F., et al. 2024, Mol. Phys., 122, e2182612
Le Petit, F., Ruaud, M., Bron, E., et al. 2016, A&A, 585, A105
Lípari, S., Díaz, R., Taniguchi, Y., et al. 2000, AJ, 120, 645
Lira, P., Ward, M., Zezas, A., Alonso-Herrero, A., & Ueno, S. 2002, MNRAS,
   330, 259
Lutz, D., Sturm, E., Janssen, A., et al. 2020, A&A, 633, A134
Maloney, P. R., Hollenbach, D. J., & Tielens, A. G. G. M. 1996, ApJ, 466, 561
McCall, B. J., Geballe, T. R., Hinkle, K. H., & Oka, T. 1999, ApJ, 522, 338
McCall, B. J., Hinkle, K. H., Geballe, T. R., et al. 2002, ApJ, 567, 391
Miller, S., Tennyson, J., Geballe, T. R., & Stallard, T. 2020, Rev. Mod. Phys., 92
Mizus, I. I., Alijah, A., Zobov, N. F., et al. 2017, MNRAS, 468, 1717
Nardini, E., Risaliti, G., Watabe, Y., Salvati, M., & Sani, E. 2010, MNRAS, 405,
Neufeld, D. A., & Wolfire, M. G. 2017, ApJ, 845, 163
Ohyama, Y., Terashima, Y., & Sakamoto, K. 2015, ApJ, 805, 162
Oka, T. 2013, Chem. Rev., 113, 8738
Oka, T., & Epp, E. 2004, ApJ, 613, 349
Oka, T., Geballe, T. R., Goto, M., et al. 2019, ApJ, 883, 54
Osterbrock, D. E., & Martel, A. 1993, ApJ, 414, 552
Padovani, M., Ivlev, A. V., Galli, D., & Caselli, P. 2018, A&A, 614, A111
Padovani, M., Ivlev, A. V., Galli, D., et al. 2020, Space. Sci. Rev., 216, 29
Papadopoulos, P. P. 2010, ApJ, 720, 226
Pereira-Santaella, M., Alonso-Herrero, A., Santos-Lleo, M., et al. 2011, A&A,
   535, A93
Pereira-Santaella, M., Spinoglio, L., Busquet, G., et al. 2013, ApJ, 768, 55
Pereira-Santaella, M., Spinoglio, L., van der Werf, P. P., & Piqueras López, J.
   2014, A&A, 566, A49
Pereira-Santaella, M., Colina, L., García-Burillo, S., et al. 2020, A&A, 643, A89
Pereira-Santaella, M., Colina, L., García-Burillo, S., et al. 2021, A&A, 651, A42
Pereira-Santaella, M., Álvarez-Márquez, J., García-Bernete, I., et al. 2022, A&A,
   665, L11
Pereira-Santaella, M., González-Alfonso, E., García-Bernete, I., García-Burillo,
   S., & Rigopoulou, D. 2024, A&A, 681, A117
Perna, M., Arribas, S., Catalán-Torrecilla, C., et al. 2020, A&A, 643, A139
Perna, M., Arribas, S., Pereira Santaella, M., et al. 2021, A&A, 646, A101
Ricci, C., Privon, G. C., Pfeifle, R. W., et al. 2021, MNRAS, 506, 5935
Rich, J., Aalto, S., Evans, A. S., et al. 2023, ApJ, 944, L50
Rodriguez-Gomez, V., Genel, S., Vogelsberger, M., et al. 2015, MNRAS, 449,
Shaw, G., & Ferland, G. J. 2021, ApJ, 908, 138
Teng, S. H., Rigby, J. R., Stern, D., et al. 2015, ApJ, 814, 56
Trafton, L. M., Geballe, T. R., Miller, S., Tennyson, J., & Ballester, G. E. 1993,
   ApJ, 405, 761
van der Tak, F. F. S., Black, J. H., Schöier, F. L., Jansen, D. J., & van Dishoeck,
  E. F. 2007, A&A, 468, 627
van der Werf, P. P., Isaak, K. G., Meijerink, R., et al. 2010, A&A, 518, L42
Veilleux, S., Rupke, D. S. N., Kim, D.-C., et al. 2009, ApJS, 182, 628
Veilleux, S., Meléndez, M., Sturm, E., et al. 2013, ApJ, 776, 27
Vivian, U., Lai, T., Bianchin, M., et al. 2022, ApJ, 940, L5
Wolfire, M. G., Vallini, L., & Chevance, M. 2022, ARA&A, 60, 247
Wright, G. S., Rieke, G. H., Glasse, A., et al. 2023, PASP, 135, 048003
  Instituto de Física Fundamental, CSIC, Calle Serrano 123, 28006
  Madrid, Spain
```

Indriolo, N., Fields, B. D., & McCall, B. J. 2009, ApJ, 694, 257

Iwasawa, K., Sanders, D. B., Teng, S. H., et al. 2011, A&A, 529, A106+

Indriolo, N., & McCall, B. J. 2012, ApJ, 745, 91

Universidad de Alcalá, Departamento de Física y Matemáticas, Campus Universitario, 28871 Alcalá de Henares, Madrid, Spain

³ Centro de Astrobiología (CAB), CSIC-INTA, Camino Bajo del Castillo s/n, E-28692 Villanueva de la Cañada, Madrid, Spain

Department of Physics, University of Oxford, Keble Road, Oxford OX1 3RH, UK

Department of Astronomy, University of Florida, P.O. Box 112055,
 Gainesville, FL 32611, USA

Gainesvine, FE 32011, GSA
 Dipartimento di Fisica e Astronomia, Università di Firenze, Via G. Sansone 1, 50019 Sesto F.no, (Firenze), Italy

⁷ INAF – Osservatorio Astrofisco di Arcetri, largo E. Fermi 5, 50127 Firenze, Italy

⁸ Centro de Astrobiología (CAB), CSIC-INTA, Ctra de Torrejón a Ajalvir, km 4, 28850 Torrejón de Ardoz, Madrid, Spain

⁹ School of Sciences, European University Cyprus, Diogenes street, Engomi, 1516 Nicosia, Cyprus

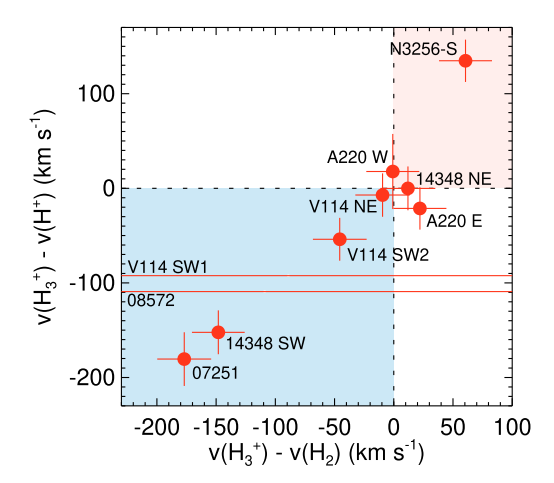


Fig. A.1. Comparison between the velocity measured for the H_3^+ absorptions and that of H_2 (x axis) and H recombination lines (y axis). For two objects, no H_2 lines are available, so the horizontal line marks the H_3^+ velocity relative to that of the H recombination lines. The shaded blue and red areas indicate blue and red velocity shifts, respectively.

Table A.1. Sample of local (U)LIRGs.

Object	Region	<i>D</i> _L ^(a) (Mpc)	$\log L_{ m IR}/L_{\odot}{}^{(a)}$	$\log L_{ m 2-10keV}^{ m obs} ^{(b)} \ ({ m ergs}^{-1})$	Ref. ^(b)	AGN (c)	Ref. ^(c)
VV 114 E	SW-s1	85.5	11.71			No/Obs.?	D23, R23, B24
	$SW-s2^{(\dagger)}$						B24, GA24
	NE			41.02	G06	No/Obs.?	D23, R23, B24
IRAS 05189-2524	nucleus	188	12.10	43.79	I11	Type 2	P21
IRAS 07251-0248	E nucleus	400	12.45	40.09	I11, R21	No/Obs.	P21, PS21
IRAS 08572+3915	NW nucleus	261	12.15	41.31	I11, R21	LINER	V13
IRAS 09111-1007	W nucleus	242	12.05	40.50	I11	LINER?	D97
NGC 3256	N nucleus	38.9	11.64	40.39	L02	No	L00
	S nucleus			39.73	L02	No/Obs.	O15
	outflow(*)						•••
IRAS 13120-5453	nucleus	136	12.27	41.86	R21	Type 2	P21
IRAS 14348-1447	NE nucleus	375	12.41	41.12	R21	LINER?/Obs.?	P21, PS21
	SW nucleus			41.53	R21	LINER?/Obs.	P21, PS21
Arp 220	W nucleus	78	12.19	40.77	C02	LINER	P20
	E nucleus			40.64	C02	LINER	P20
II Zw 096	D1	161	11.94	41.32	I11	No/Obs.?	I22, GB24
	C0 ^(‡)						
	$D0^{(\ddagger)}$						
IRAS 22491-1808	E nucleus	352	12.23	40.65	I11	No/Obs.	P21, PS21
NGC 7469	nucleus	70.8	11.65	43.73	B03, PS11	Type 1	O93, U22, A23, B24

Notes. $^{(a)}$ Luminosity distance and 8-1000 μ m IR luminosity from Armus et al. (2009) and Pereira-Santaella et al. (2021). $^{(b)}$ Observed 2–10 keV X-ray luminosity and reference. $^{(c)}$ AGN classification based on optical spectroscopy and references. Obs. indicates dust obscured AGN based on indirect evidences from the mid-IR and sub-mm. "?" indicates inconclusive classification. $^{(\dagger)}$ SW-s2 is located \sim 100 pc away from the nucleus SW-s1. The highly excited CO and H₂O mid-IR absorptions of this region were analyzed by González-Alfonso et al. (2024) and Buiten et al. (2024). (*) This region encompasses the collimated molecular outflow launched by the southern nucleus of NGC 3256. It is located \sim 110 pc away from the nucleus and corresponds to region N1 of Pereira-Santaella et al. (2024). (*) These two regions of II Zw 096 are bright star-forming clumps located 0.5–1 kpc from the nucleus D1 (Inami et al. 2022).

References. (A23) Armus et al. 2023; (B03) Blustin et al. 2003; (B24) Bianchin et al. 2024; (B24) Buiten et al. 2024; (C02) Clements et al. 2002; (D23) Donnan et al. 2023; (D97) Duc et al. 1997; (G06) Grimes et al. 2006; (GA24) González-Alfonso et al. 2024; (GB24) García-Bernete et al. 2024b; (I11) Iwasawa et al. 2011; (I22) Inami et al. 2022; (L00) Lípari et al. 2000; (L02) Lira et al. 2002; (O93) Osterbrock & Martel 1993; (O15) Ohyama et al. 2015; (P20) Perna et al. 2020; (P21) Perna et al. 2021; (PS11) Pereira-Santaella et al. 2011; (PS21) Pereira-Santaella et al. 2021; (R21) Ricci et al. 2021; (R23) Rich et al. 2023; (U22) Vivian et al. 2022; (V13) Veilleux et al. 2013.

Appendix A: Sample and data reduction

We selected all the (U)LIRGs with publicly available high spectral resolution NIRSpec and Mid-Infrared Instrument (MIRI) spectroscopic observations in the JWST archive by July 2024. We excluded few objects, mainly interacting systems whose nuclei are not clearly separated at the angular resolution of JWST/MIRI at \sim 20 μ m, which is needed for the continuum modeling of each nuclei. The final sample consists of 12 systems (see Table A.1) with data from the Director's Discretionary Early Release Science

Table B.1. EW of the H₂⁺ R-branch transitions and derived column densities.

Target	R(3,3) ^u	N(3,3)	R(3,3) ^l	N(3,3)	R(1,0) (a)	N(1,0)	R(1,1) ^l	N(1,1)
	$3.427 \mu\text{m}$ $(10^{-5} \mu\text{m})$	(10^{15}cm^{-2})	$3.534 \mu\text{m}$ $(10^{-5} \mu\text{m})$	(10^{15}cm^{-2})	3.669 μm (10 ⁻⁵ μm)	(10^{15}cm^{-2})	$3.715 \mu\text{m}$ $(10^{-5} \mu\text{m})$	$(10^{15}\mathrm{cm}^{-2})$
VV 114 SW-s1	3.5 ± 0.8	3.5 ± 0.8	6.5 ± 0.7	2.3 ± 0.3	5.2 ± 0.6	1.3 ± 0.2	16.4 ± 0.6	7.6 ± 0.3
VV 114 SW-s2	<3.1	<3.1	5.9 ± 1.4	2.1 ± 0.5	12.1 ± 1.1	3.1 ± 0.3	11.6 ± 1.0	5.4 ± 0.5
VV 114 NE	<2.3	<2.3	<1.2	< 0.42	7.5 ± 1.1	1.9 ± 0.3	6.2 ± 1.1	2.9 ± 0.5
IRAS 07251(*)	<10.5	<10.5	< 5.1	<1.8	26.9 ± 3.8	6.8 ± 1.0		
IRAS 08572	<3.4	< 3.4			10.5 ± 0.6	2.7 ± 0.2	3.8 ± 0.6	1.8 ± 0.3
NGC 3256-S	<4.9	<4.9	10.2 ± 1.2	3.6 ± 0.4	18.5 ± 0.6	4.7 ± 0.1	18.8 ± 0.5	8.7 ± 0.2
IRAS 14348 NE(*)	< 5.5	< 5.4	< 2.5	< 0.90	15.7 ± 2.1	4.0 ± 0.5		
IRAS 14348 SW ^(*)	< 6.8	< 6.8	< 3.2	<1.1	14.5 ± 2.6	3.7 ± 0.7	< 2.4	<1.1
Arp 220 W	<1.6	<1.6	2.0 ± 0.7	0.70 ± 0.27	10.1 ± 0.7	2.6 ± 0.2	4.5 ± 0.7	2.1 ± 0.3
Arp 220 E	<4.0	<4.0	5.5 ± 1.6	2.0 ± 0.6	14.9 ± 1.1	3.8 ± 0.3	10.8 ± 1.0	5.0 ± 0.5
IRAS 05189	<2.0	<2.0	<2.0	< 0.70	<1.9	< 0.48	<1.9	< 0.87
IRAS 09111	< 5.4	< 5.4	< 5.7	< 2.0	< 5.7	<1.5	< 5.6	< 2.6
NGC 3256-N	<3.1	<3.1	<3.4	<1.2	<3.5	< 0.90	< 3.5	<1.6
IRAS 13120	<2.2	<2.2	< 2.0	< 0.71	<1.8	< 0.47	<1.8	< 0.83
II Zw 096 C0	<3.6	<3.6	<3.8	<1.3	<3.7	< 0.95	<3.8	<1.7
II Zw 096 D0	<3.8	<3.8	<4.0	<1.4	<4.0	<1.0	< 3.9	<1.8
NGC 7469	< 2.0	< 2.0	< 2.0	< 0.70	<1.9	< 0.49	<1.9	< 0.88

Notes. (a) The R(1,0) 3.669 μ m and R(1,1)^u 3.668 μ m transitions are blended for these objects. To determine the W_{λ} of R(1,0), the contribution of R(1,1)^u was estimated from the W_{λ} of R(1,1)^l. (*) For these objects it was not possible to measure R(1,1)^l, thus the listed R(1,0) W_{λ} value includes the contributions from both R(1,0) and R(1,1)^u.

(DD-ERS) Program #1328 (PI: L. Armus and A. Evans), the Large Program #3368 (PI: L. Armus and A. Evans), and the Guaranteed Time Observations Program #1267 (PI: D. Dicken; Program lead: T. Böker).

These objects were observed with the high spectral resolution NIRSpec grating G395H using the integral field unit (IFU) mode (Böker et al. 2022). The G395H grating has a resolving power, R, between 1900 and 3600, and covers the spectral range between 2.87 and 5.27 μ m (JWST User Documentation). Between ~3.5 μ m and ~4.3 μ m, the spectral range where the H_3^+ band is observed, R varies between 2400 and 3000. JWST/MIRI observations of these objects were also available for all the bands of the Medium Resolution Spectrograph (MRS; Wright et al. 2023; Argyriou et al. 2023) between 4.9 and 28.1 μ m with R=2300–3700 (Labiano et al. 2021).

For the data reduction, we used the JWST calibration pipeline (version 1.12.4; Bushouse et al. 2023) and the context 1253. We followed the standard reduction recipe complemented by a number of custom steps to mitigate the effect of bad pixels and cosmic rays on the extracted spectra. Further details on the data reduction of the NIRSpec and MIRI/MRS data observations can be found in Pereira-Santaella et al. (2022, 2024) and García-Bernete et al. (2022b, 2024a).

We extracted the spectra of 20 regions within these systems. Sixteen regions correspond to their nuclei, three regions are bright near-IR clumps with strong bursts of star-formation (Inami et al. 2022; García-Bernete et al. 2024b; Buiten et al. 2024), and one region samples the spatially resolved molecular outflow of NGC 3256-S (Pereira-Santaella et al. 2024; Table A.1). We applied an aperture correction to the spectra similar to García-Bernete et al. (2022c).

Appendix B: Properties of the H_3^+ absorptions

The EW of the detected H_3^+ absorptions and upper limits are listed in Tables B.1, B.2, and B.3, for the R, Q, and P branches, respectively. Table B.4 shows the total H_3^+ column densities.

Table B.2. EW of the H_3^+ Q-branch transitions and derived column densities.

Target	Q(3,3)	N(3,3)	$Q(2,2)^{(a)}$	<i>N</i> (2,2)	Q(1,1)	<i>N</i> (1,1)	Q(1,0)	<i>N</i> (1,0)	$Q(2,1)^l$	<i>N</i> (2,1)	Q(3,0)	N(3,0)
	3.904 μm (10 ⁻⁵ μm)	$(10^{15}\mathrm{cm}^{-2})$	$3.914 \mu m$ $(10^{-5} \mu m)$	$(10^{15}\mathrm{cm}^{-2})$	$3.929 \mu\text{m}$ $(10^{-5} \mu\text{m})$	$(10^{15}\mathrm{cm}^{-2})$	3.953 μm (10 ⁻⁵ μm)	(10^{15}cm^{-2})	3.971 μm (10 ⁻⁵ μm)	$(10^{15}\mathrm{cm}^{-2})$	3.986 μm (10 ⁻⁵ μm)	$(10^{15}\mathrm{cm}^{-2})$
VV 114 SW-s1	2.4 ± 0.5	2.3 ± 0.4	<1.6	<1.2	7.9 ± 0.5	3.8 ± 0.2						
VV 114 SW-s2	5.1 ± 1.1	4.9 ± 1.0			10.9 ± 1.0	5.2 ± 0.5	18.8 ± 1.0	4.5 ± 0.2	<3.4	<1.2		
VV 114 NE			<1.1	< 0.78	4.6 ± 1.1	2.2 ± 0.5	11.2 ± 1.0	2.7 ± 0.3	<1.0	< 0.38	<3.6	< 0.89
IRAS 07251	26.5 ± 4.3	25.4 ± 4.1	17.0 ± 4.2	12.2 ± 3.0	31.5 ± 4.1	15.2 ± 2.0	53.9 ± 3.8	13.0 ± 0.9	20.4 ± 3.7	7.4 ± 1.3	16.3 ± 3.6	4.0 ± 0.9
IRAS 08572							8.9 ± 1.3	2.1 ± 0.3	3.0 ± 1.2	1.1 ± 0.4		
NGC 3256-S			<2.1	<1.5	27.9 ± 0.7	13.4 ± 0.3	18.9 ± 0.7	4.6 ± 0.2	< 0.67	< 0.24		
IRAS 14348 NE	<1.3	<1.3			9.4 ± 1.3	4.5 ± 0.6	12.5 ± 1.3	3.0 ± 0.3	<1.3	< 0.46	<1.2	< 0.30
IRAS 14348 SW	12.0 ± 1.4	11.4 ± 1.4	6.2 ± 1.4	4.4 ± 1.0	8.0 ± 1.4	3.9 ± 0.7	24.7 ± 1.3	6.0 ± 0.3	17.6 ± 1.3	6.4 ± 0.5	12.5 ± 1.3	3.1 ± 0.3
Arp 220 W	8.6 ± 2.1	8.3 ± 2.0	7.8 ± 2.1	5.6 ± 1.5	14.8 ± 2.0	7.1 ± 1.0	13.1 ± 2.0	3.2 ± 0.5	< 2.0	< 0.74	< 2.0	< 0.49
Arp 220 E	8.4 ± 2.1	8.0 ± 2.0	<2.1	<1.5	16.9 ± 2.0	8.1 ± 1.0	21.3 ± 2.0	5.2 ± 0.5	< 2.0	< 0.72	<1.9	< 0.47
IRAS 05189									<1.6	< 0.58	<1.6	< 0.40
IRAS 09111							<7.4	<1.8	<7.1	< 2.6	<7.2	<1.8
NGC 3256-N			< 3.2	<2.3	< 3.2	<1.5	< 3.2	< 0.76	< 3.2	<1.2	< 3.2	< 0.78
IRAS 13120												
II Zw 096 C0												
II Zw 096 D0												
NGC 7469	< 2.0	< 2.0					<2.1	< 0.50	<2.1	< 0.77	< 2.1	< 0.52

Notes. (a) The Q(2,2) 3.914 μ m and Q(2,1)^u 3.916 μ m transitions are blended for these objects. The Q(2,1)^u absorption is ~4 times fainter than the Q(2,1)^l, so only for IRAS 07251 and IRAS 14348 SW, where the Q(2,1)^l absorption is detected, we used its W_{λ} to estimate the Q(2,1)^u contribution.

Table B.3. EW of the H₂⁺ P-branch transitions and derived column densities.

Target	P(1,1) (a)	N(1,1)	P(2,2) (b)	N(2,2)	P(3,3)	N(3,3)	P(3,0)	N(3,0)
	$4.070 \mu m$ $(10^{-5} \mu m)$	$(10^{15}\mathrm{cm}^{-2})$	4.204 μm (10 ⁻⁵ μm)	$(10^{15}\mathrm{cm}^{-2})$	4.350 μm (10 ⁻⁵ μm)	(10^{15}cm^{-2})	$4.355 \mu m$ $(10^{-5} \mu m)$	$(10^{15}\mathrm{cm}^{-2})$
VV 114 SW-s1	7.9 ± 0.7	5.5 ± 0.5	< 0.67	< 0.25	8.3 ± 0.6	2.5 ± 0.2	< 0.65	< 0.48
VV 114 SW-s2			6.4 ± 1.3	2.4 ± 0.5	17.0 ± 1.1	5.1 ± 0.3	<3.8	< 2.8
VV 114 NE			<1.0	< 0.37	7.1 ± 0.9	2.1 ± 0.3	< 0.89	< 0.66
IRAS 07251			45.7 ± 2.8	17.0 ± 1.0	107.5 ± 2.0	32.2 ± 0.6	18.3 ± 2.0	13.7 ± 1.5
IRAS 08572			5.7 ± 0.8	2.1 ± 0.3	9.2 ± 0.7	2.7 ± 0.2	2.1 ± 0.7	1.6 ± 0.5
NGC 3256-S			6.5 ± 3.5	2.4 ± 1.3	12.7 ± 3.1	3.8 ± 0.9	<3.1	<2.3
IRAS 14348 NE			<1.9	< 0.70	9.9 ± 1.2	3.0 ± 0.4	<1.2	< 0.90
IRAS 14348 SW			24.8 ± 2.5	9.2 ± 0.9	70.3 ± 2.1	21.1 ± 0.6	12.0 ± 2.1	9.0 ± 1.6
Arp 220 W			13.6 ± 3.3	5.1 ± 1.2	42.5 ± 2.9	12.7 ± 0.9	< 2.9	<2.2
Arp 220 E	•••	•••	11.4 ± 3.7	4.2 ± 1.4	32.1 ± 3.3	9.6 ± 1.0	<3.4	<2.5
IRAS 05189			<1.6	< 0.59	<1.5	< 0.46	<1.5	<1.1
IRAS 09111			<12.2	<4.5	<12.8	<3.8	<12.9	< 9.6
NGC 3256-N			< 3.7	<1.4	<3.8	<1.1	<3.8	<2.8
IRAS 13120			<2.1	< 0.77	< 2.0	< 0.61	< 2.0	<1.5
II Zw 096 C0			<4.6	<1.7	<4.8	<1.4	<4.8	< 3.6
II Zw 096 D0			<3.3	<1.2	< 3.2	< 0.94	<3.1	<2.3
NGC 7469			<1.9	< 0.69	<1.8	< 0.55	<1.8	<1.4

Notes. $^{(a)}$ The P(1,1) transition is blended with the H₂ 1-1 S(13) 4.068 μ m. Thus, for most objects it is not possible to derive realiable measurements or upper limits. $^{(b)}$ The P(2,2) transition is affected by the CO₂ ice and gas absorptions in some cases (e.g., NGC 3256-S), so the derived EW and column densities for this transition are uncertain.

Table B.4. Column densities of H₃⁺ and H.

Target	$N({\rm H_3^+})^{(a)}$ $(10^{15}{\rm cm^{-2}})$	$N(1,1)^{(b)}$ $(10^{15} \mathrm{cm}^{-2})$	$N(1,0)^{(b)}$ $(10^{15} \text{ cm}^{-2})$	$N(2,2)^{(b)}$ (10 ¹⁵ cm ⁻²)	$N(2,1)^{(b)}$ (10 ¹⁵ cm ⁻²)	$N(3,3)^{(b)}$ $(10^{15} \mathrm{cm}^{-2})$	$N(3,0)^{(b)}$ $(10^{15} \text{ cm}^{-2})$	$N_{\rm H}^{(c)}$ (10 ²² cm ⁻²)	$N({\rm H_3^+})/N_{\rm H} \stackrel{(d)}{}$ (10^{-7})
VV 114 SW-s1	9.7 ± 2.0	5.6 ± 1.9	1.3 ± 0.2	<1.2		2.8 ± 0.7		4.9	2.0
VV 114 SW-s2	16.4 ± 1.3	5.2 ± 0.5	3.8 ± 1.0	2.4 ± 0.5		5.0 ± 0.5	< 2.8		
VV 114 NE	7.0 ± 0.6	2.2 ± 0.5	2.7 ± 0.3	< 0.78	< 0.38	2.1 ± 0.3	< 0.89	13.2	0.53
IRAS 07251	92.7 ± 6.6	15.2 ± 2.0	13.0 ± 0.9	14.6 ± 3.4	7.4 ± 1.3	28.8 ± 4.8	13.7 ± 1.5	18.9	4.9
IRAS 08572	11.7 ± 0.9	1.8 ± 0.3	2.4 ± 0.4	2.1 ± 0.3	1.1 ± 0.4	2.7 ± 0.2	1.6 ± 0.5	12.1	0.97
NGC 3256-S(*)	21.8 ± 1.0	13.4 ± 0.3	4.6 ± 0.1	<1.5	< 0.24	3.8 ± 0.9	<2.3	13.1	1.7
IRAS 14348 NE	10.5 ± 0.8	4.5 ± 0.6	3.0 ± 0.3	< 0.70	< 0.46	3.0 ± 0.4	< 0.90	10.9	0.96
$IRAS~14348~SW^{(\dagger)}$	80.2 ± 5.9	3.9 ± 0.7	6.0 ± 0.3	4.4 ± 1.0	6.4 ± 0.9	11.4 ± 1.4	3.1 ± 0.3	14.7	5.5
Arp 220 W	28.0 ± 1.9	7.1 ± 1.0	3.2 ± 0.5	5.1 ± 1.2	< 0.74	12.7 ± 0.9	< 0.49	17.2	1.6
Arp 220 E	27.1 ± 2.0	8.1 ± 1.0	5.2 ± 0.5	4.2 ± 1.4	< 0.72	9.6 ± 1.0	<2.5	15.6	1.7
IRAS 05189	<1.8	< 0.83	< 0.48	< 0.59	< 0.58	< 0.46	< 0.40	5.6	< 0.32
IRAS 09111	< 7.9	< 2.5	<1.6	<4.5	< 2.6	< 3.8	< 5.7	5.6	<1.4
NGC 3256-N	<4.2	<1.5	< 0.83	<1.8	<1.2	<1.8	<1.8	1.7	< 2.5
IRAS 13120	< 2.0	< 0.83	< 0.47	< 0.77		< 0.66	<1.5	6.1	< 0.32
II Zw 096 C0	<4.7	<1.7	< 0.95	<1.7		< 2.1	<3.6		
II Zw 096 D0	<4.8	<1.7	<1.0	<1.2		< 2.1	<2.3		
NGC 7469	< 2.0	< 0.84	< 0.49	< 0.69	< 0.77	< 0.62	< 0.52	5.0	< 0.39

Notes. ^(a) Total column density of H_3^+ estimated by summing the population of the measured H_3^+ levels in this table. We did not correct this total column density from the ~10–50% H_3^+ molecules in unobserved metastable levels, which depends on the physical conditions and excitation of the H_3^+ clouds (Appendix D and Oka et al. 2019). The upper limits are derived from the upper limits of the three lowest metastable levels of H_3^+ : (1,1), (1,0), and (3,3). ^(b) Adopted column density for the H_3^+ levels (1,1), (1,0), (2,2), (2,1), (3,3), and (3,0). We averaged the columns from the different branches, excluding, in most cases, those derived from the R branch due to the dilution by the stellar continuum of the R branch (Sect 2.3). We also excluded some absorptions partially blended with emission lines in some of the objects (e.g., Q(3,3) in Arp 220). ^(c) H column density estimated from the extinction affecting the 3.4–4.4 µm continuum (see Sect. 3.1; Donnan et al. 2024). The estimated uncertainty is ~0.3 dex. ^(d) H_3^+ fractional abundance. The uncertainty is dominated by the 0.3 dex uncertainty on $N_{\rm H}$. ^(*) In NGC 3256-S the P(2,2) transition is detected (Table B.3 and Fig. C.1), but its EW is affected by the broad CO₂ ice and gas absorptions. For this reason, we adopt the upper limit estimated from the Q(2,2) transition. ^(†) For IRAS 14348 SW, the P-branch column densities are 2.3±0.6 times larger than those from the Q branch. Thus, we considered the Q-branch values for the column of the individual levels, which are used for population ratios, and obtained the total column density by multiplying their sum by 2.3.

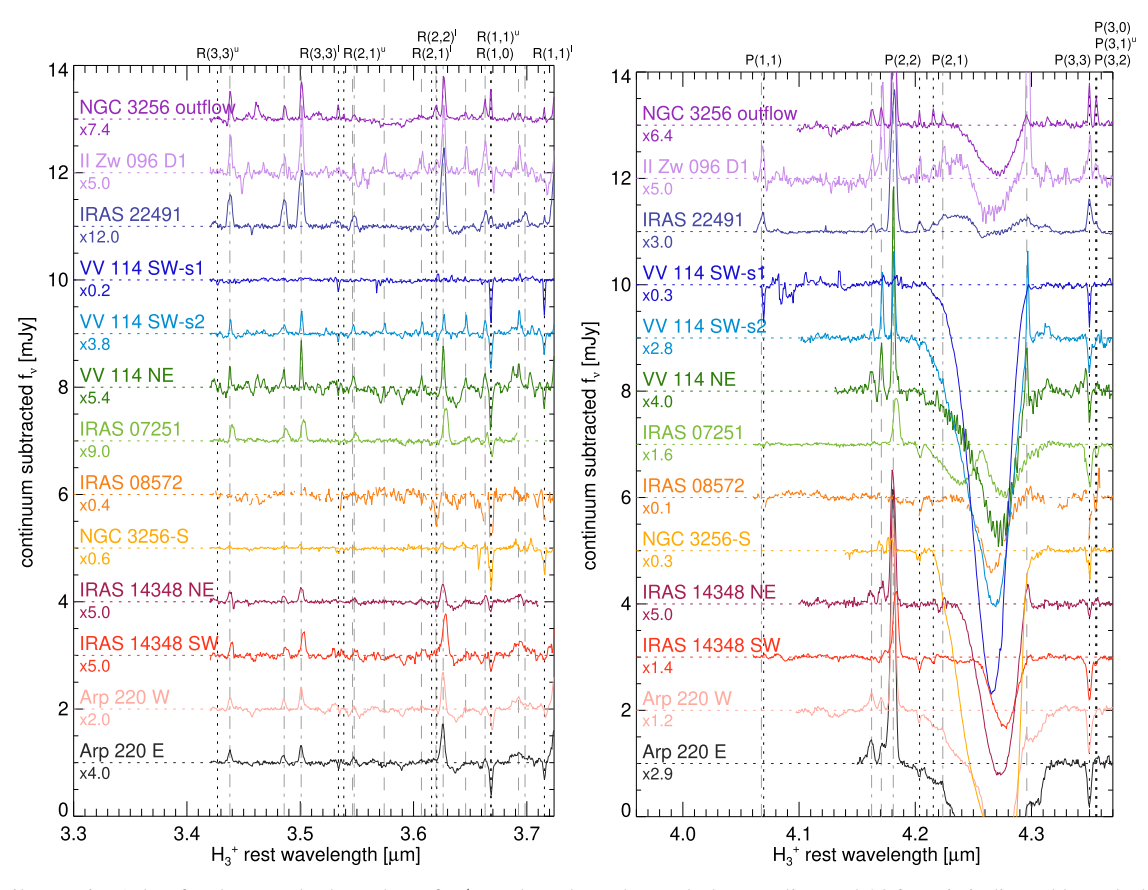


Fig. C.1. Similar to Fig. 1, but for the R and P branches of H_3^+ . In the P-branch panel, the He I line at $4.296\,\mu m$ is indicated by a dashed gray line.

Appendix C: Spectra of the ${\rm H_3^+}$ band

Figure C.1 presents the R and P branches of the detected H_3^+ band. The Q branch is shown in Fig. 1. Figure C.2 shows the spectra of the regions where no H_3^+ is detected.

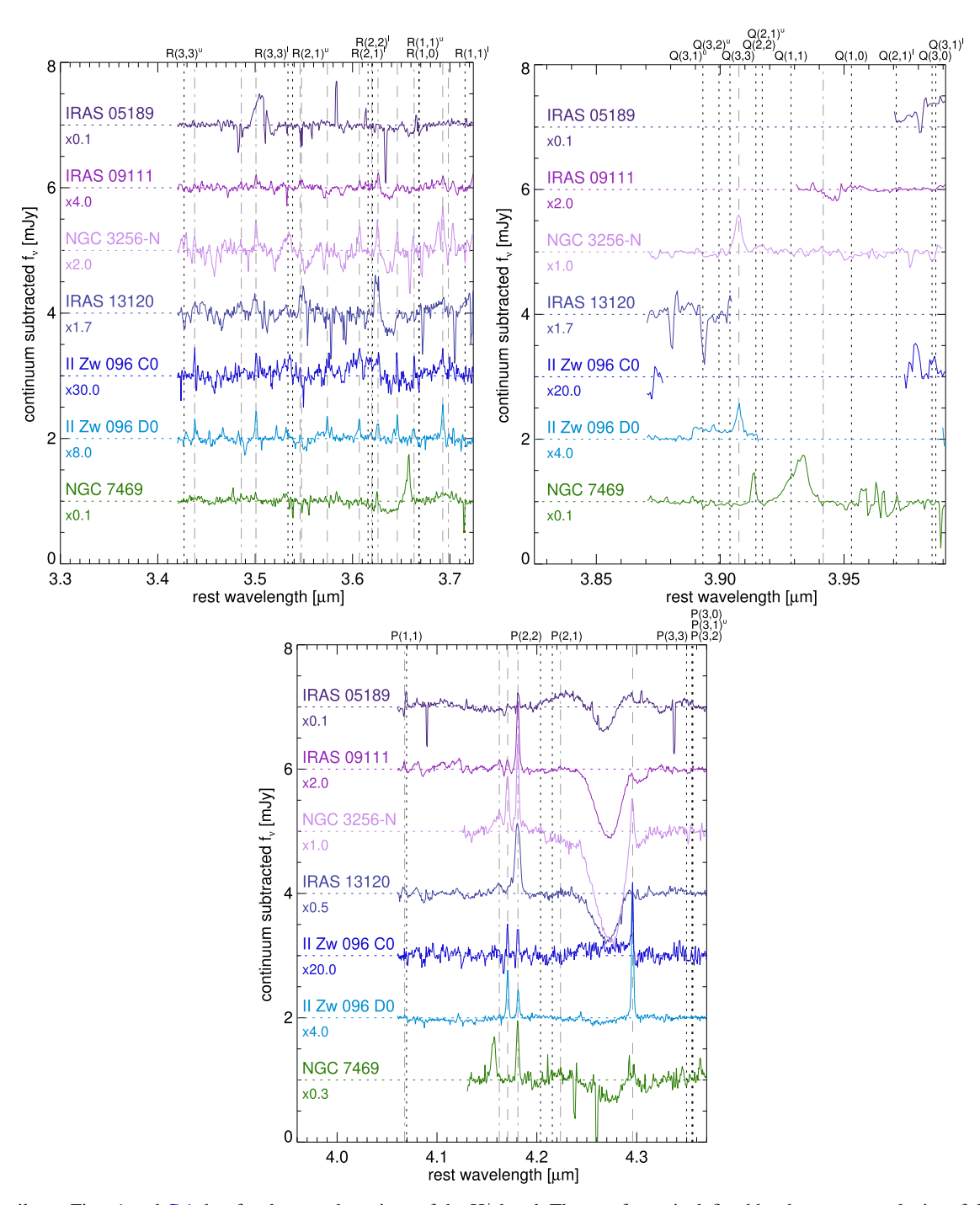


Fig. C.2. Similar to Figs. 1 and C.1, but for the non-detections of the H_3^+ band. The rest frame is defined by the average velocity of the H_2 and H transitions.

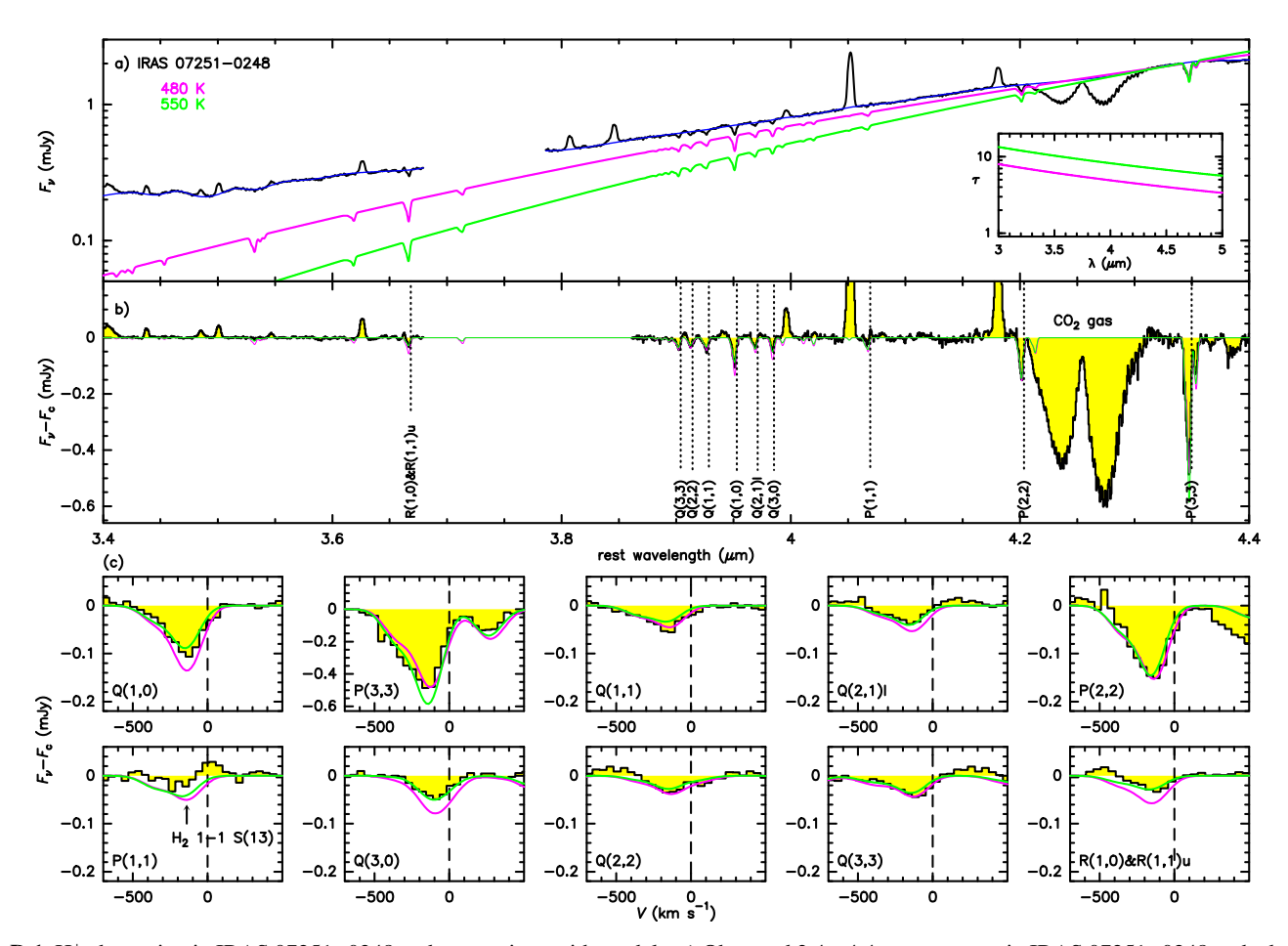


Fig. D.1. H_3^+ absorption in IRAS 07251–0248 and comparison with models. a) Observed 3.4 – 4.4 μ m spectrum in IRAS 07251–0248 and adopted spline-interpolated baseline (in blue). The magenta and green lines show the modeled spectra, with the temperatures of the central source T_c and the hot-dust optical depth (τ in the inset) also indicated with colors. b) The continuum-subtracted spectrum (yellow histogram) is compared with the predictions by the two models. The spectra and models for individual lines are plotted in units of velocity in panel c. The vertical dashed line indicates the rest-frame zero velocity determined from the H_2 and H_1 lines. The position of the H_2 1 – 1 S(13) 4.068 μ m line, which is blended with the P(1,1) 4.070 μ m line, is indicated by an arrow.

Appendix D: Models of the $H_{\mathfrak{J}}^+$ absorptions including IR pumping

We have modeled the H_3^+ absorption in IRAS 07251–0248 and IRAS 14348–1447 SW using the code described in González-Alfonso et al. (1998). The models assume spherical symmetry with the statistical equilibrium of the H_3^+ level populations calculated within a shell of gas surrounding a mid-IR source of continuum radiation. The spectra are computed towards the IR source excluding reemission from the flanks. The effects of both radiative pumping by the IR source and collisional excitation are included. The varying parameters are the equivalent radius and temperature of the central source (R_c and T_c), the extinction by the dust mixed with the H_3^+ (assuming an extinction law with $\tau_{\lambda} \propto \lambda^{-1.7}$), the H_3^+ column density of the shell ($N(H_3^+)$), the distance between the H_3^+ shell and central source (d), the gas conditions (n_{H_2} and n_{K_1}), and the gas velocity field. We assume that the dust mixed with the gas is cold enough such that its reemission does not contribute to the < 4.3 μ m continuum.

Figures D.1 and D.2 show the $3.4-4.4\,\mu m$ spectra of IRAS 07251-0248 and IRAS 14348-1447 SW, with the blue lines indicating the adopted spline-interpolated baselines. As discussed in Sect. 2.3, H_3^+ line absorption is progressively diluted in the stellar continuum at shorter wavelengths, and hence we attempt different spectral shapes for the hot-dust emission characterized by T_c and $\tau_{4\mu m}$; R_c is then determined by assuming negligible stellar continuum at 4.35 μm (see Donnan et al. 2024). We show in Figs. D.1 and D.2 two models, A (in magenta) and B (in green), with T_c , τ_{λ} and the hot-dust emission indicated in panel a. In these figures, the continuum-subtracted spectra in both sources is compared with the predictions by the two models, and details of the observed and modeled line shapes are shown in panels c. The physical parameters of the models are listed in Table D.1.

These models show that, including IR pumping, it is possible to reproduce the absorptions from the (3,0) and (2,1) levels, which are difficult to explain just by collisional excitation with H_2 (Sect. 3.2).

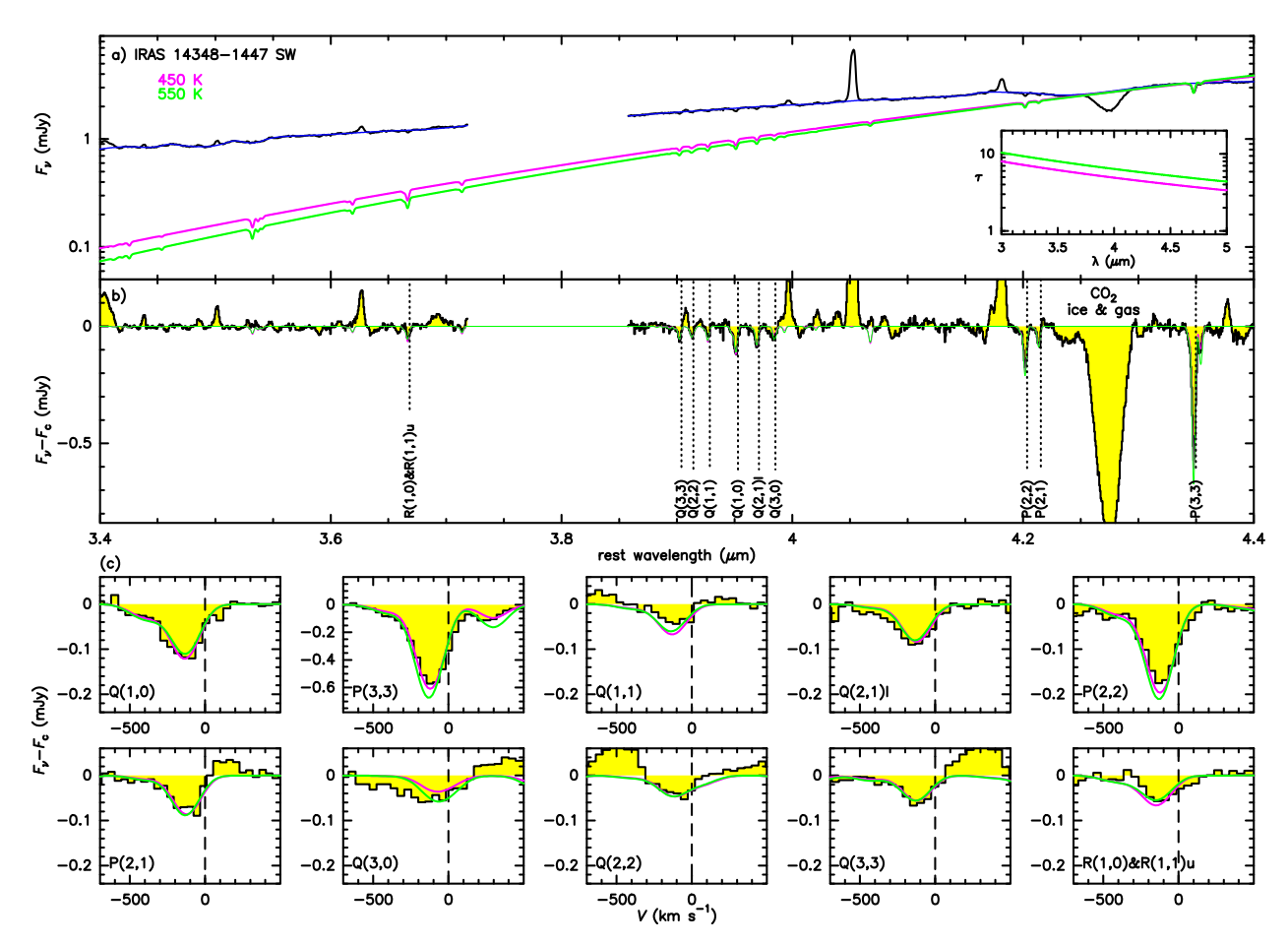


Fig. D.2. Same as Fig. D.1 but for IRAS 14348–1447 SW.

Table D.1. Parameters for the models shown in Figs. D.1 and D.2.

Source	Model	<i>T_c</i> (K)	R _c (pc)	$ au_{4\mu\mathrm{m}}$	d (R_c)	$N({\rm H_3^+})$ $(10^{17}{\rm cm^{-2}})$
IRAS 07251-0248	A (magenta) B (green)	480 550	4.8 10.9	5.0 8.3	1.05 4.0	1.8 1.8
IRAS 14348-1447 SW	A (magenta) B (green)	450 550	5.9 5.7	5.0 6.4	16 16	0.82 1.0